Introduction

These four lectures describe quantum dots in various regimes from large dots containing perhaps several thousand electrons, to small dots containing 0,1,2... electrons. The interest in these systems is the ability to control electrons, often one at a time, in a regime in which quantum interference, electron-electron interaction and chaotic classical dynamics combined. Because electron numbers can range from 0 to tens of thosands, these systems are well-suited to explore problems at the heart of mesoscopics, namely, the crossover from microscopic to macroscopic, from, from discrete to continuous, from coherent to classical.

The focus of these talks will be principally toward experimental results, with occasional pointers to the theoretical literature, as I know it. No doubt, I will leave out crucial references both to relevant theory and to complementary experiments from other groups. I apologize up front for that. The primary probes of these systems is transport, i.e. measuring the current-voltage characteristics of these devices in response to various external conditions. In part of Lecture 3 and Lecture 4, I will mention charge sensing as an alternative way of measuring what is going on inside the dot.

Lecture 1. Mesoscopic Quantum Dots

The structures described are fabricated on a two dimensional electron gas (2DEG) wafer (material grown by our collaborators) consisting of epitaxial layers of AlGaAs and GaAs, as shown in Figs. 1-3. Typical device parameters for the 2DEG are given in table 1. Notice that even for moderate mobilities, the electron transport mean free path exceeds the typical device size by at least an order of

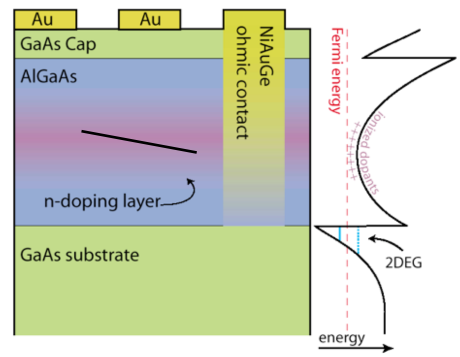

Fig. 1 View of the heterostructure along the growth direction, showing 2DEG and surface gates.

magnitude. Devices are fabricated using electron beam lithography, following several steps of photolithograph during which ohmic contacts are applied, larger gate stuctures deposited, and alignment marks placed. Following these lithographic steps, the device is bonded into a commercial chip carrier (custom made by Kyocera to contain no nickel), which inserts into a chip carrier socket (also made with no nickel, see Fig. 3) and cooled in a dilution refrigerator. The various fridges around the lab use a common strategy for keeping the electrons cool. The dc lines pass through ~1-10kΩ resistors that divide isolated segments of a metallic enclosure—usually the hollow core of the cold-finger is used for this purpose—which provides both thermal sinking through the resistors and electromagnetic isolation. Isolating coaxial lines for high-frequency operation involves many more tricks and will be discussed briefly below, in the section on ac transport.

Depending on the impedance of the device, we use either a four-wire lock-in measurement, best suited for the moderate impedance (~10kΩ) of open quantum dots and quantum point contacts (QPC's) or a two-wire current measurement (usually using an Ithaco 1211 preamplifier) for higher-impedance (~1MΩ)

2DEG Property	Symbol	Value	Units
Effective mass	m^*	0.067	$m_e = 9.1 \times 10^{-28}$ g
Spin degeneracy	g_s	2	
Valley degeneracy	g_v	1	
Dielectric constant	ε	13.1	$\varepsilon_0 = 8.9 \times 10^{-12}$ Fm^{-1}
Effective Lande g-factor	g^*	–0.44	
Density of states	$\rho(E) = g_s g_v (m^*/2\pi\hbar^2)$	2.8×10^{10}	cm^{-2}meV^{-1}
Level spacing	$1/\rho(E)$	3.57	μeVμm^2
Fermi wave vector	$k_F = (4\pi n_s/g_s g_v)^{1/2}$	1.1×10^6	cm^{-1}
Fermi energy	$E_F = (\hbar k_F)^2/2m^*$	7.0	meV
		81	K
Fermi wavelength	$\lambda_F = 2\pi/k_F$	56	nm
Fermi velocity	$v_F = \hbar k_F/m^*$	1.9×10^7	cm/s
Scattering time	$\tau = m^* \mu_e/e$	40	ps
Mean free path	$l = v_F \tau$	10	μm
Resistivity	$\rho = (n_s e \mu_e)^{-1}$	30	Ω per square
Diffusion constant	$D = v_F^2 \tau/2$	7×10^4	cm^2/s
Thermal diffusion length	$l_T = (\hbar D/kT)^{1/2}$	5×10^3	nm/$\sqrt{T}$
Cyclotron energy	$\hbar\omega_c$	1.73	meV/B
		20	K/B
Cyclotron radius	$l_c = \hbar k_F/eB$	70	nm/B
Magnetic length	$l_m = (\hbar/eB)^{1/2}$	26	nm/$\sqrt{B}$
Zeeman energy	$g^* \mu_B B$	25.5	μeV/B
		296	mK/B

Table 1 Typical values for a GaAs/AlGaAs 2DEG. Density and mobility are taken to be $n_s = 2\times10^{11}$ cm-2 and $\mu_e = 1\times10^6$ cm^2/Vs, with dependent quantities scaling as indicated. Magnetic field, *B*, is in tesla, and temperature, *T*, is in kelvin.

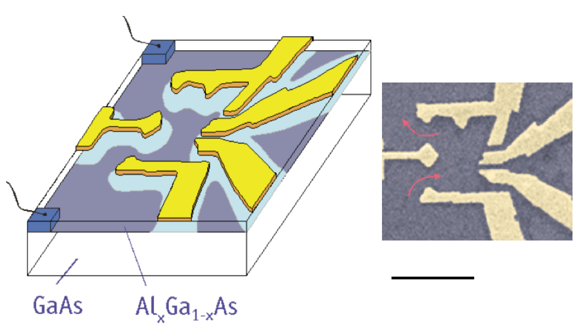

Fig. 2 Left: Schematic view of a quantum dot, defined by gates on the surface of the 2DEG. The electrons are depleted under the gates (light blue). Right: electron micrograph with false color, showing a quantum dot containing ~ 1000 electrons. Scale bar is 1 μm.

devices, as found for instance in the Coulomb blockade regime.

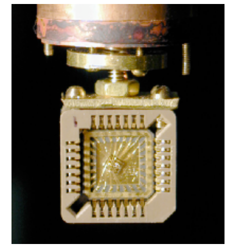

Fig. 3 The GaAs chip is glued to the chip carrier socket and bonded. The carrier is then inserted into the socket that is mounted on the fridge.

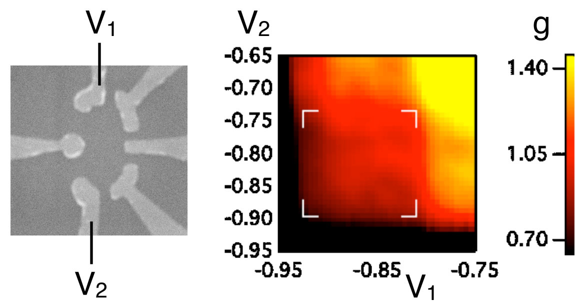

Fig. 4 Left: Gate voltages V_1 and V_2 are used to control the coupling of the dot to the reservoirs. Right: Colorscale of dot conductance g, in units of e^2/h. A plateau in dot conductance at ~ $1e^2/h$ is seen (in the red square) when QPC 1 and QPC 2 are each on plateaus of conductance $2e^2/h$.

The dots are connected to the reservoirs by quantum point contact leads that can be individually adjusted to give the desired conductance. It is easy to recognize plateaus in conductance of the QPC leads, even when measuring though the full device, so setting the leads, for instance to an integer number of quantized conduction modes is rather straightforward.

Typical low-temperature behavior of the dot conductance in the open regime, $g > 2e^2/h$ is shown in Fig. 5.[1] Important features to notice are large, aperiodic conductance fluctuations as a function of magnetic field, symmetric in field and sensitive to changes in the shape of the dot (as controlled by voltages on the confining potentials. These fluctuations are of the

[1] M. Switkes, Ph.D. thesis. Available at http://marcuslab.harvard.edu.

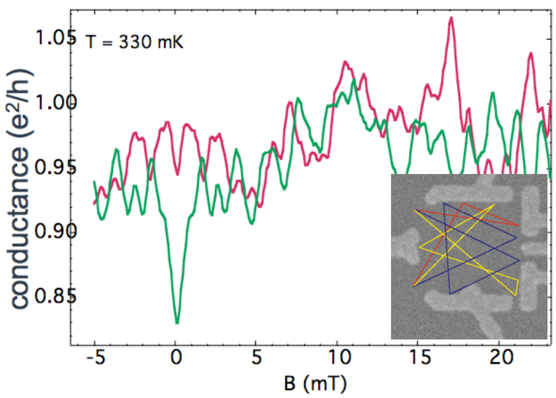

Fig. 5 Typical conductance fluctuations as a function of magnetic field at two different device shapes. Note symmetry in field. Inset: Micrograph of the quantum dot, with colored trajectories suggesting various ballistic paths, arising from diffraction at the QPC. Interference between these paths can be thought of as the origin of the magnetic field fluctuations.

same origin as universal conductance fluctuations in disordered mesoscopic metallic samples, namely, interference of multiple paths passing through the device.

The symmetry in magnetic field, B, applied perpendicular to the plane of the 2DEG is a consequence of the Landauer-Büttiker symmetry for a two-lead device, $R_{ij,ij}$ (B) =$R_{ij,ij}$(-B). Even though the device is measured in a four-wire configuration, the majority of the voltage is dropped across the device, which is a two-lead device.

The trajectories depicted in the micrographs in the insets of Figs. 5 and 6, are of course schematic, but reflect a semiclassical view of ballistic transport. From this kind of analysis much can be learned, including, for instance, the functional form of the correlation function (or equivalently, the power spectrum) of these fluctuations. Another theoretical approach is

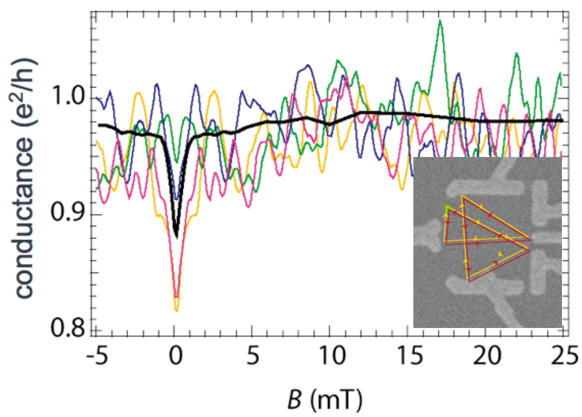

Fig. 6 Colored traces show conductance fluctuations for various devices shapes (controlled by gate voltages defining the confining potential of the dot). The black trace is the average of ~100 such traces. The magnetic field dependence in the average is lost, except for the dip at B=0, due to coherent backscattering. The size of the dip can be used to measure dephasing time. Inset: Dot micrograph, showing time-reversed pairs of ballistic trajectories that contribute to coherent backscattering, resulting in a lowering of average conductance when all time-reversed pairs interfere constructively.

random matrix theory (RMT) which applies in the case of chaotic classical dynamics within the dot.[2] The beautiful, interconnected story of RMT, level repulsion, and conductance fluctuations has been reviewed in the literature[2] and will not be summarized here. Instead, we take only the results we need to allow conductance fluctuations to be used to learn about the dephasing time $\tau_\varphi(T)$.

Whereas the rms amplitude of conductance fluctuations depends on $\tau_\varphi(T)$ as well as T explicitly, the weak localization correction, appearing as a dip at zero magnetic field in the *average* conductance, is only temperature dependent through $\tau_\varphi(T)$. In fact, RMT models that include dephasing through the inclusion of voltage-probe leads allow $\tau_\varphi(T)$ to be

[2] For review of RMT as applied to quantum dots, see C. W. J. Beenakker, Reviews of Modern Physics **69**, 731 (1997); Y. Alhassid, Reviews of Modern Physics **72**, 896 (2000). For a review of RMT in disordered systems, see the text by P. Mello, Oxford University Press.

weak localization correction

$$\delta g \simeq \frac{e^2}{h}\frac{N}{2N+1+\gamma_\varphi}$$

conductance fluctuations

$$var(g) = \frac{\Delta}{6kT} f(\gamma_\varphi),$$

$$f(\gamma_\varphi) = \frac{2}{2+\gamma_\varphi}\,\frac{1}{(\sqrt{3}+\gamma_\varphi)^2}$$

dephasing channels

$$\gamma_\varphi \;=\; 2\pi\hbar/(\tau_\varphi\Delta)$$

mean level spacing

$$\Delta \;=\; 2\pi\hbar^2/m^* A_{\mathrm{dot}}$$

Table 2 Random matrix theory formulas for weak localization correction and variance conductance fluctuations (in units of e^2/h). Weak localization formula is valid for any number of modes in each lead, N > 1, whereas the approximate formula for conductance fluctuations is valid for N=1 only. Various forms of these expressions, valid in various limits are known.

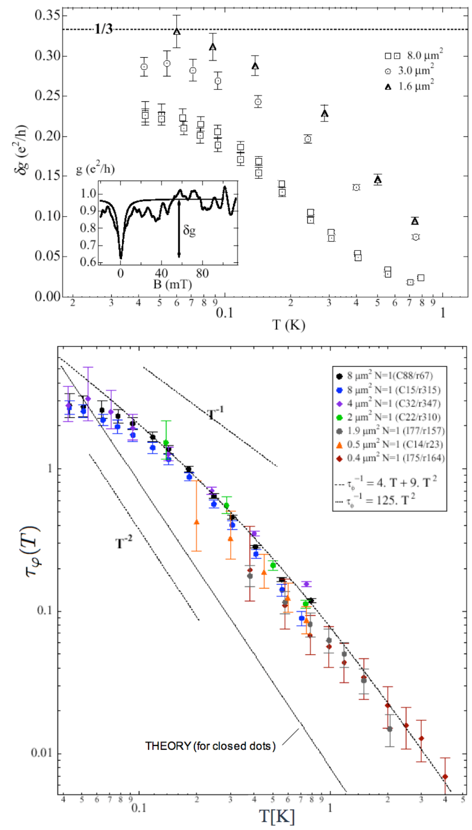

Fig. 7 Top: Weak localization as a function of temperature for three different size devices. The smallest device shows full (zero temperature) weak localization, whereas the larger devices show depressed weak localization. This is because the number of dephasing channels increases for a given τ_φ as the size increases, see Table 2. Bottom: Phase coherence time extracted from weak localization for quantum dots ranging over a factor of 20 in area collapse to the same curve. The curve that appears to fit the data except at the lowest temperatures is a combination of T and T^2 dependence of τ_φ^{-1}, similar to what is seen in disordered 2D systems. Perhaps that is the appropriate theory?

extracted directly from $\delta g = \langle g(B{\neq}0)\rangle - \langle g(B{=}0)\rangle$, with formulas that depend only on the number of quantum channels connecting the dot to the reservoirs, and the area of the dot, A_{dot}, which determines its mean level spacing. Formulas for the case of single-mode leads are given in Table 2.[3]

The measured dephasing time $\tau_\varphi(T)$ measured from these formulas (or ones like them, depending on experimental parameters) is show in Fig. 8. Two features are worth noting: the first is that over much of the measured range, $\tau_\varphi(T) \propto 1/T$. This result disagrees with relevant theory (which predicts $\tau_\varphi(T) \propto 1/T^2$). [4] However, the theory addressed closed devices, explicitly disallowing scattering with momentum transfer smaller than the inverse dimension of the dot.[4] The second thing to notice is that the data appears to saturate at low temperature. As was demonstrated in Ref

[3] A. G. Huibers, et al., Phys. Rev. Lett. **83**, 5070 (1999); A. Huibers, Ph.D. thesis, available at http://marcuslab.harvard.edu

[4] U. Sivan, Y. Imry, and A. G. Aronov, Europhys. Lett. **28**, 115 (1994).

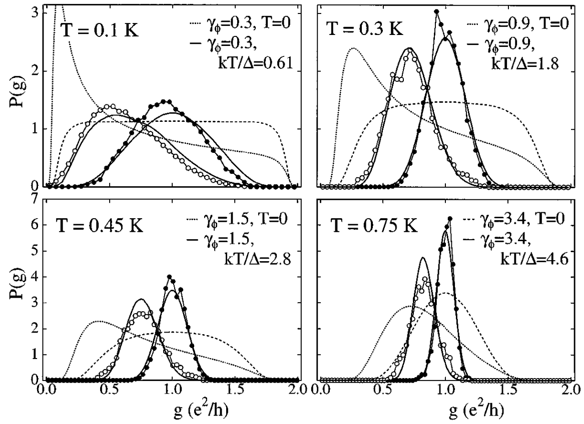

Fig. 8 Full distributions of conductance fluctuations, showing good agreement between theory and experiment, once theory has accounted for finite temperature and dephasing (solid curves). Dashed curves show dephasing effects only (T = 0).

4, this saturation is not the result of a saturating electron temperature. Here, the explicit temperature dependence of var(g) is useful as a thermometer: we see a continued ~ $1/T$ rise in var(g) between 100 mK and 40mK.

It is interesting to note that RMT predicts not just the mean and variance of conductance fluctuations, but the full distribution function, P(g). This is perhaps the best illustration of the universality of RMT. The distribution of conductances is not dependent on material (as long as spin-orbit effects are weak, though that too can be accounted for, as discussed below), device shape (as long as it generates classical chaos), or size (except insofar is area affects γ_φ through Δ). Only the temperature, dephasing rate, and number of channels in the leads are parameters of the theory. As seen in Fig. 8, the experimental distributions are in good agreement with theory, once finite temperature and dephasing are included in the theory.[5]

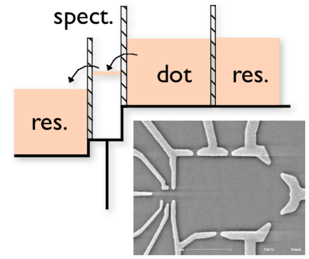

Fig. 9 Large quantum dot with single-electron dot acting as energy spectrometer. Differential conductance through the spectrometer measures the wave function in the dot at the location of the spectrometer at a fixed energy below the Fermi surface of the dot, set by the gate voltage. This systems allows a measurement of dephasing along the scar (see text).

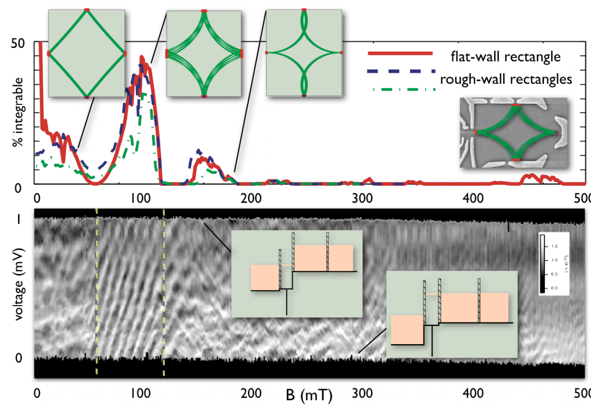

Fig. 10 Lower panel shows conduction from the big dot through the spectrometer dot(grayscale), as a function of magnetic field and voltage of the spectrometer relative to the Fermi surface of the dot, i.e., 0 corresponds to the spectrometer on the Fermi surface. The window of strong diagonal stripes between ~ 50-120 mT corresponds to a region where a focusing condition gives a strong diamond shaped scar of a periodic orbit. Top panel: percent of classical phase space associated with periodic orbits (the rest being chaotic) as a function of magnetic field (for rectangular billiard the size of the dot.

[5] A. G. Huibers, et al., Phys. Rev. Lett. **81**, 1917 (1998).

amplitude of Nth harmonic:

$$A_{Nf}(\varepsilon) = A_0 \exp\left(-Nt \cdot \tau^{-1}(\varepsilon)\right)$$

period of one cycle:

$$t = L / v_F \quad \sim 18 \text{ ps}$$

ratio of first harmonic to second harmonic:

$$\frac{A_f(0)}{A_{2f}(0)} = \exp(t\tau_{esc}^{-1})$$

from fit to power spectrum of g in striped region:

$$\tau_{esc} \sim 17\text{ps}$$

model all energy dependence as reflecting dephasing

$$\tau^{-1}(\varepsilon) = \tau_{esc}^{-1} + \tau_{\varphi}^{-1}(\varepsilon)$$

find zero-energy value from weak localization

$$\tau_{\varphi}(0) \sim 2 \text{ ns} >> \tau_{esc}$$

Table 3 Model for extracting energy dependent dephasing from the amplitude of periodic oscillations.

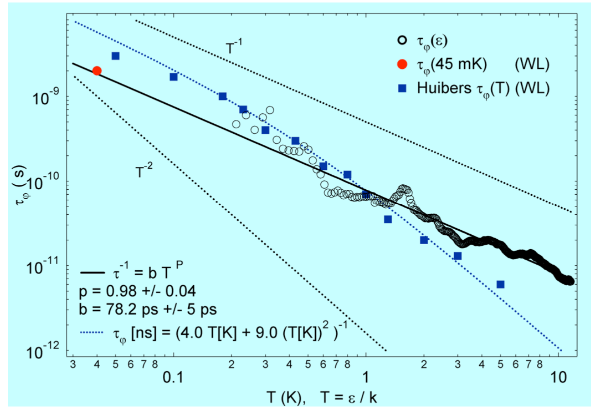

Fig. 11 Dephasing rate as a function of energy off of the Fermi surface of the large dot (black circles). By defining an effective temperature $T = \varepsilon/k_B$ we can compare $\tau_\varphi(\varepsilon)$ from the spectroscopic measurement to $\tau_\varphi(T)$ from weak localization. The two compare surprisingly well, with the notable lack of a T^{-2} part in the $\tau_\varphi(\varepsilon)$, perhaps because the substrate remains at base temperature.

Deviations from RMT have been investigated in transport measurement, and have been associated theoretically with self-similar structure in conductance fluctuations. The experimental evidence[6] for self-similar, or fractal, conductance fluctuations is not firmly established in my opinion.

Following work by Sivan[7] and coworkers, we have constructing a spectrometer using a small dot adjacent to a big dot, as seen in Fig. 9.[8] Differential conductance dI/dV measured through the single electron dot serves as a spectrometer of the large dot, giving a measure of the wave function of the large dot at the location of the spectrometer at an energy set by the energy level of the single-electron dot relative to the Fermi sea of the large dot. In the magnetic field range ~50-120 mT a strong series of ridges appears in the data (Fig. 10). Classical phase space analysis of a simplified version of the problem shows that a strong periodic orbit with a concave diamond develops within the dot in this range of magnetic field. The spacing of the stripes in the data correspond well to the expected period Aharonov-Bohm oscillations with an area given by the diamond, while the slope of the stripes agrees with the expected dependence in the field-energy plane to keep the number of wavelengths around the orbit constant on each stripe.

It is evident by inspection that the oscillations, and overall conductance fluctuations, are stronger when the spectrometer is near the Fermi surface of the large dot (toward the bottom of the bottom panel of Fig. 10). Assuming the interpretation of the stripe features to be valid, we can use energy-dependent amplitude of the periodic oscillations to extract a energy dependent dephasing rate, $\tau_\varphi(\varepsilon)$, where ε is the distance of the spectrometer window (the single particle level) below the Fermi

[6] J. P. Bird, J. Phys.-Condes. Matter **11**, R413 (1999).

[7] U. Sivan, et al., Europhys. Lett. **25**, 605 (1994).

[8] D. M. Zumbuhl, Ph.D. thesis, available at http://marcuslab.harvard.edu and in preparation.

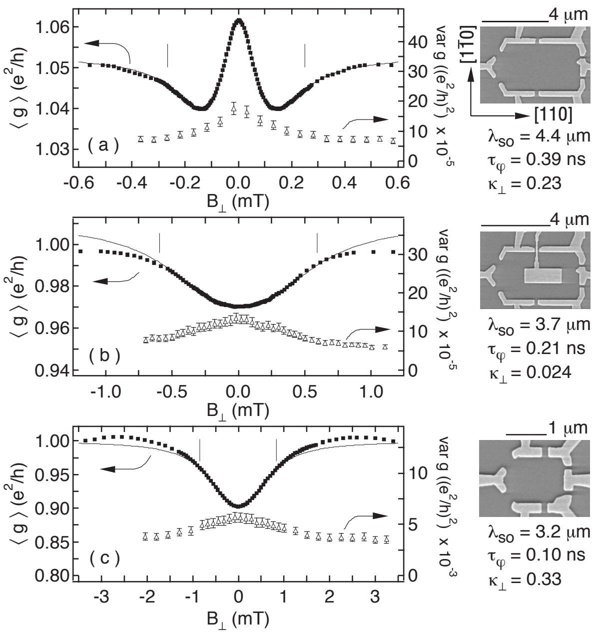

Fig. 12 Average conductance $\langle g \rangle$ (squares) and variance of conductance var(g) (triangles) calculated from 200 statistically independent samples, generated by shape averaging, as a function of perpendicular magnetic field $B_\perp$ for (a) 8.0 µm² dot (b) 5.8 µm² center-gated dot and (c) 1.2 µm² dot at T = 0.3K, along with fits to RMT (solid curves). In (b), the center gate is fully depleted. When the center gate is undpleted, this device shows antilocalization. Vertical lines indicate the fitting range, error bars of $\langle g \rangle$ are about the size of the squares. Note that the large dot shows antilocalization (a peak in conductance at B = 0) while the small dot, made of the same material, shows weak localization, demonstrating how the effects of spin-orbit coupling are suppressed by confinement.

surface of the dot. The procedure is outlined in Table 3, and the results shown in Fig. 11. If we make the connection to previous measurements of $\tau_\varphi(T)$ through the simple association $\varepsilon \leftrightarrow T$ (without the 3.5 from the derivative of the Fermi function), then, remarkably, the data from this experiment sits essentially on top of the weak localization data. The data also has a slope $\tau_\varphi(\varepsilon) \propto 1/T$, in this case extending across a broader temperature range. Theory also exists to extract $\tau_\varphi(\varepsilon)$ from the chaotic parts of phase space, but that analysis has not yet been carried out.

λ_1, λ_2	SO length along crystal axes
$\lambda_{so} = \sqrt{\lambda_1 \cdot \lambda_2}$	average SO length
$\nu_{so} = \sqrt{\lambda_1 / \lambda_2}$	SO anisotropy
γ_φ	decoherence rate
κ	geometry dependent constant

spin-orbit parameters

$$a_x^2 = \pi\kappa \frac{E_T}{\Delta}\left(\frac{A}{\lambda_1\lambda_2}\right)^2 \quad \text{(AB like SO term)}$$

$$a^2 = \left(\left(\frac{L_1}{\lambda_1}\right)^2 + \left(\frac{L_2}{\lambda_2}\right)^2\right) a_x^2 \quad \text{(spin flips)}$$

$$h^2 = \frac{\pi}{2}\left(\frac{E_Z}{\Delta}\right)^2 \left(\frac{\Delta}{E_T}\right)\left(\frac{L}{\lambda_{so}}\right)^2 \quad (\text{SO} + B_{||})$$

magnetic fields

$$x^2 = \pi\kappa\left(\frac{E_T}{\Delta}\right)\left(\frac{2eB_\perp A}{h}\right)^2 \quad \text{perpendicular}$$

$$b = \pi\frac{g\mu_B B_{||}}{\Delta} \quad \text{parallel}$$

Table 4 Device parameters that determine the symmetry class within RMT. See Table 5 below

	weak $B_{||}$ $b, h^2 \ll N+\gamma_\varphi$	intermed. $B_{||}$ $h^2 \ll N+\gamma_\varphi \ll b$	strong $B_{||}$ $N+\gamma_\varphi \ll h^2, b$
weak SO $a^2, a_x^2 \ll N+\gamma_\varphi$	4 s=2 Σ=1	2	1
intermediate SO $a^2 \ll N+\gamma_\varphi \ll a_x^2$	2 s=1 Σ=1	1	1
strong SO $N+\gamma_\varphi \ll a^2, a_x^2$	1 s=1 Σ=2	1	1

Table 5 Chart of parameter ranges for RMT including Zeeman and spin-orbit effects. The large numbers in each square characterize the relative size of var (g) ~ s/(βΣ).

So far, there has been no mention of the spin of the electron. In material with weak spin-orbit coupling, we can consider either RMT or semiclassical formulations that ignore spin. As the strength of spin-orbit coupling increases, spin effects on quantum interference become dramatic. This is, of course, well known from the mesoscopics of bulk disordered metals and semiconductors, where, for instance, weak localization effects *change sign* in the presence of strong. The origin of this change of sign in quantum corrections to average conductivity is the fact that as an electron spins evolves through 2π (for instance, by following the motion of the electron around a loop due to spin-orbit coupling), its overall wave function of the electron undergoes a sign change, and it takes a rotation by 4π to bring the sign back to its original. This change in sign reverses the sign of coherent backscatter to *destructive* interference producing a peak, rather than a dip, in conductance, at zero magnetic field (where all loops interfere).

In heterostructure-based quantum dots, the dominant spin-orbit effects show an important cancelation effect due to the winding and unwinding of spin rotations associated with the confined motion of electrons in zero dimensions. The cancellation, which applies only to Rashba-type and linear Dresselhaus spin-orbit coupling eliminates the first-order contribution, but leaves second order effects, which take the form of a spin dependent Aharonov-Bohm effect. Higher-order term (in the quantity (L/λ_{so}) where L is a typical linear dimension of the device, and λ_{so} is roughly the length over which the spin rotates by 2π due to spin-orbit coupling). An extended RMT for spin-orbit coupling in quantum dots, including Zeeman fields, was given by Aleiner and Falko.[9]

The extended RMT gives the variance of conductance fluctuations (at T = 0) in terms of symmetry parameters: var (g) ~ s/($\beta\Sigma$), where β is the conventional (Dyson) parameter describing time-reversal symmetry, s is the

$$\delta g_{wl}(B_{||}) = \delta g_{RMT}(B_{||})\, f_{FJ}(B_{||})$$

$$\mathrm{var}\, g(B_{||}) = \mathrm{var}\, g_{RMT}(B_{||})\,[1 + f_{FJ}(B_{||})]$$

$$f_{FJ}(B_{||}) = \left[1 + \frac{\gamma_B}{\gamma_{esc}}\right]^{-1} \quad \gamma_{esc} = \frac{N\Delta}{h} \quad \gamma_B = a \cdot B_{||}^2 + b \cdot B_{||}^6$$

Table 6 Modifying SO+Zeeman RMT results for weak localization and variance of conductance fluctuations to include orbital coupling. This has been treated in the simplest way, by multiplying RMT result by the orbital (FJ) factor.

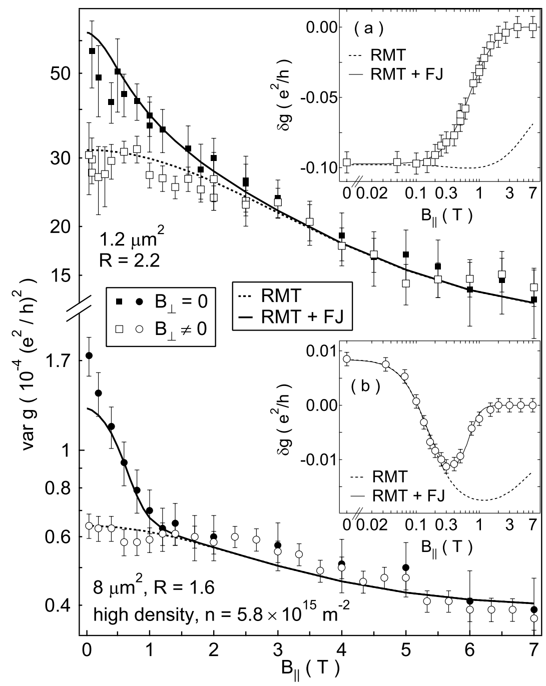

Fig. 13 Dependence of conductance fluctuations var(g) (main figure) and average conductance ⟨g⟩ (inset) measured in an 8 μm² quantum dot with single-mode leads and large spin-orbit coupling, for the case where time-reversal symmetry is unbroken (solid circles) and broken (open circles) by a perpendicular magnetic field. Theory curves are RMT with and without the inclusion of an explicit breaking.

Kramers degeneracy parameter and Σ characterizes mixing of different spins when Kramers degeneracy is already broken. Spin rotation symmetry is classified as either not

[9] I. L. Aleiner and V. I. Falko, Phys. Rev. Lett. 87, 256801 (2001); J. N. H. J. Cremers, P. W. Brouwer, I. L. Aleiner, and V. I. Fal'ko, Phys. Rev. B 68, 125329 (2003).

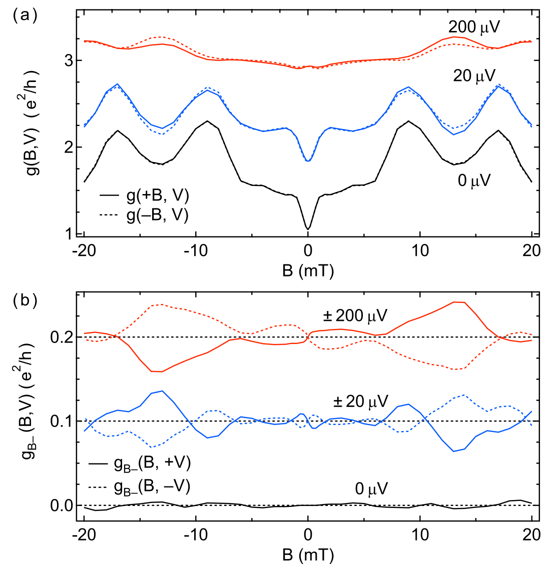

Fig. 14 (a) Differential conductance g for N = 2 modes per lead in an 8 μm² dot as a function of B (solid curves) and −B (dashed curves) at source-drain V as indicated, measured at electron temperature T = 45mK. The blue (red) curves are offset by +0.5 (+1) e²/h, respectively. (b) Antisymmetric in B conductance g_{B-} of the traces shown in (a), as a function of B at V (solid curves) and −V (dashed curves) as indicated. The blue (red) curves are offset by +0.1 (+0.2) e²/h, respectively. Black curve demonstrates Landauer-Büttiker symmetry for V = 0 and blue/red curves indicate that g_{B-} is antisymmetric in V.

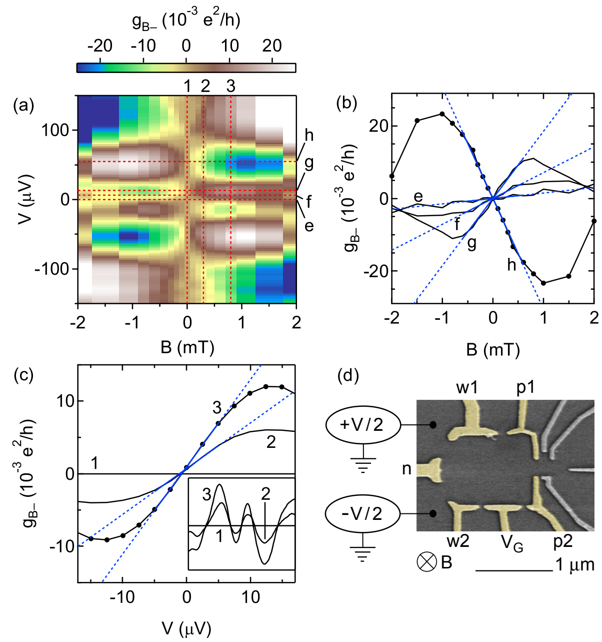

Fig. 15 (a) g_{B-} (color scale) as a function of B and V for fixed plunger V_G at N = 2. Red dashed lines indicate the locations for data shown in (b) and (c). (b) g_{B-} as a function of B at V = 0, 7.5, 15, 55 μV. (c) gB− as a function of V at B = 0, 0.3, 0.8 mT. Linear fits to curves in (b) and (c) are shown in dashed blue lines, with solid blue lines indicating the fitting range. Inset to (c) shows the same cuts as in (c) with the V axis extended to ±125 μV and the g_{B-} axis extended to ±25 × 10^{-3} e²/h. (d) Electron micrograph of a similar device. Only the yellow gates are used in this experiment. V is applied symmetrically.

broken (s = 2, Σ = 1), partially broken (s = 1, Σ = 1) or completely broken (s = 1, Σ = 2). The variance of conductance is reduced by a factor of two when a crossover into the class with next-lower symmetry occurs. The Kramers degeneracy can be lifted by a Zeeman field as well as spin-orbit coupling if $B_\perp$ = 0. Once Kramers degeneracy is broken (s = 1), mixing of spins (Σ = 2) due to spin-orbit coupling is possible at $B_\parallel = 0$ for strong spin-orbit coupling or can be induced by $B_\parallel$ when spin-orbit coupling is suppressed by confinement near $B_\parallel = 0$. Finite temperatures and decoherence strongly reduce var (g), but the relative reduction factor var$g(B_\perp = 0, B_\parallel = 0)$/ var $g(B_\perp = 0, B_\parallel \neq 0)$ is only affected weakly.

Figure 12 demonstrates the suppression of weak localization effects by confinement in high-density GaAs quantum dots.[10] These wafers happened to have a large spin-orbit coupling by virtue of the high density, which makes the Fermi velocity larger, and the details of the heterostructure interface. For large dots made from this wafer, spin-orbit effects

[10] D. M. Zumbuhl, et al., Phys. Rev. Lett. **89**, 276803 (2002). D. M. Zumbuhl, et al. PRB-RC, in press (cond-mat/ 0501622 (2005).

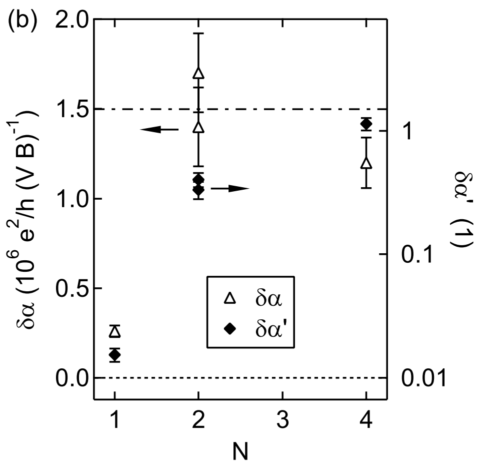

Fig. 16 Standard deviation of interaction parameter (left axis) and dimensionless interaction parameter (right axis) as a function of the number of modes in the leads. The dash-dot line indicates the theoretical estimate. Whereas theory gives a δα decreasing with the number of modes in each lead as N^{-2}, the experiment shows δα increasing. The likely explanation for this result is that the theory does not include thermalization, which occurs for small N. For larger N, the distribution of electron energies in the dot are out-of-equilibrium due to the relatively rapid escape.

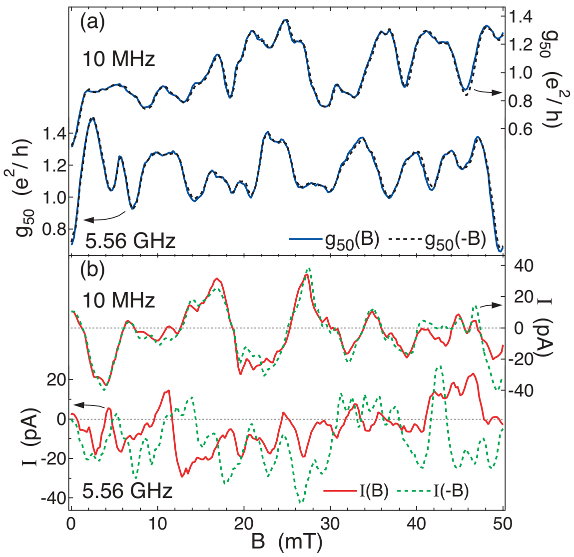

Fig. 17 (a) Modest effect of microwaves on the symmetry of conductance, shown for +B (solid blue) and -B (dashed). (b) dc current induced by the application of rf or microwave gate voltage. At 10MHz, the symmetry of the current reveals its origin to be rectification. At 5.56 GHz, there is very little symmetry in B. Here, photovoltaic effects dominate transport.

reverse the sign of coherent backscattering, giving antilocalization (a conductance peak at $B = 0$). For the small dot in Fig. 12(c), made from the same material, spin-orbit effects are suppressed by confinement and no antilocalization is observed. The device in 12(b) has an interior gate that allows it to be controllably switched from a large dot with antilocalization to a small dot with localization. One could imagine a class of devices that take advantage of rapid turning on and off of spin orbit coupling. The rapid change in area provided by the internal gating allows such a process. The solid curves in Fig. 12 are fits to RMT, showing essentially perfect agreement between theory and experiment.

The extended RMT also can account for combine spin-orbit and Zeeman coupling, the latter produced experimentally by a applying a purely in-plane field. At low in-plane fields, $B_{||} < 200$ mT , experiment and RMT agree essentially perfectly. At higher field, the fact that $B_{||}$ also couples to orbital electronic states (even for a perfectly 2DEG) needs to be accounted for. With this modification, good agreement over the full range of experimental parameters, for both average and variance of conductance, is obtained, is seen in Fig. 13. For average conductance there is essentially perfect agreement between the modified RMT (denoted RMT+FJ in Fig. 12) and experiment; for var(g) there is some minor discrepancy that is not understood.

So far we have restricted our attention linear-response transport (except for the spectrometer experiment) which, among other things, obey Landauer-Büttiker symmetry in applied magnetic field. We now consider two departures. If we apply a relatively large dc bias to a two-lead quantum dot, we are no longer guaranteed that the Landauer-Büttiker symmetry g(B) = g(-B) will be obeyed. It was recently pointed out while at large bias this symmetry is not guaranteed, that destroying it requires electron-electron interactions. The reason, simply put, is that without interaction, each energy level, E, within transport window will separately obey g(E,B) = g(E,-B), so that integrating over E to account for finite bias will not affect this symmetry.

If we consider the first departure from the even symmetry g(B) = g(-B). Expanding the current $I = g(B)V + \zeta(B)V^2 + ...$, we can expand $\zeta(B)$ = as $\zeta_0 + \alpha B + ...$ The term proportional to α is thus linear in B and even in source-drain voltage, and corresponds to a nonlinear conductance term $g_{nl}(B) = \alpha BV$. As shown in Refs. XX, α is proportional to electron-electron interaction strength.

In the mesoscopic regime, one expects (and indeed we find) that an ensemble average over shapes for field of α vanishes. We therefore characterize this quantity by its the standard deviation, $\delta\alpha$. We investigate the component of conductance that is antisymmetric in B, denoted $g_{B-} = (g(B) - g(-B))/2$, and extract the component linear in B, as shown in Fig. 15. After gathering statistics on these nonlinear components, we are able to find $\delta\alpha$ and its dimensionless counterpart $\delta\alpha'$, defined

$$\delta\alpha = \delta\alpha' \frac{1}{N^2}\frac{e}{\Delta}\frac{A}{\phi_0}\frac{e^2}{h} \quad ,$$

where N is the number of modes in each lead, A is the device area, φ_0 is the flux quantum. The quantity $\delta\alpha'$ has been calculated in the limit of perfect screening, with a predicted value $\pi/2$. Experimental values are in reasonable agreement for N=4, but for smaller N,

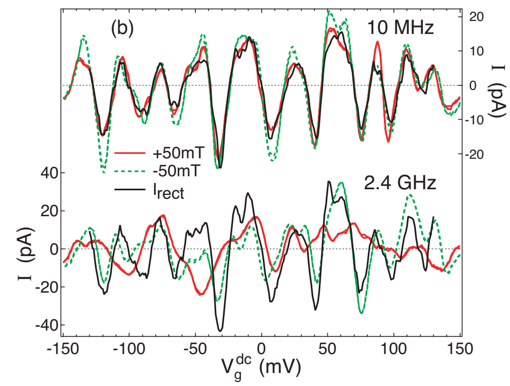

Fig. 18 Rectification model (black) describes the gate-induced fluctuations in rectification current induced by 10MHz, but does not describe the photocurrent induced by 5.56GHz, which also is asymmetric in field. The rectification calculation is based on the data at +50 mT.

where equilibration occurs within the dot before the escape time, asymmetry is reduced (as expected).

Another instance of nonlinearity that violates magnetic field symmetry is the appearance of both rectification and photovoltaic effects in quantum dots. Both effects produce dc current in response to an applied ac gate voltage. Depending on the frequency and strength of ac voltages, components that are both symmetric and antisymmetric in magnetic field appear.[11]

Rectification produces a dc current in response to a single ac applied gate voltage. It arises when a voltage applied to a gate,

$$V_g(t) = V_g^{dc} + V_g^{ac}\sin(\omega t)$$

parasitically couples to the source drain voltage, with a possible phase shift,

$$V_{ds}(t) = \alpha V_g^{ac}\sin(\omega t{+}\phi)$$

leading to an induced dc current

$$I_{\rm rect} = \frac{\omega}{2\pi}\int_0^{2\pi/\omega} \alpha V_g^{ac}\sin(\omega t+\phi) g(V_g(t))dt$$

11 L. DiCarlo, C. M. Marcus, and J. S. Harris, Jr., Phys. Rev. Lett. **91**, 246804 (2003); M. G. Vavilov, L. Dicarlo, C. M. Marcus, Phys. Rev. B 74, 341309(R) (2005).

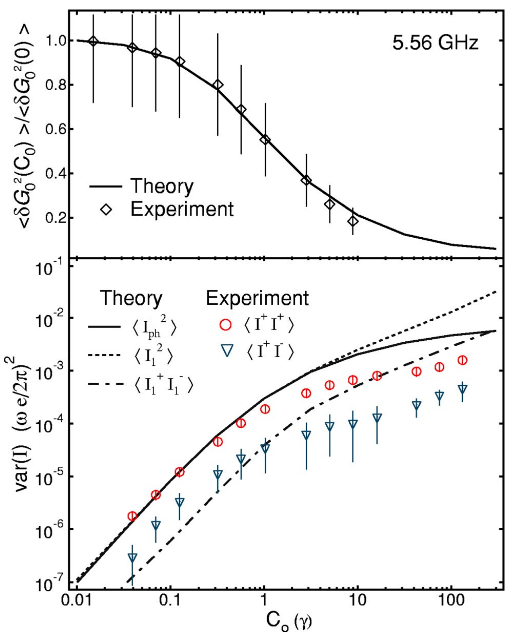

Fig. 19 (a) Variance of conductance fluctuations, in the presence of microwaves, normalized by the zero-power variance. Fitting theory to the data allows the power parameter C_0 to be calibrated. (b) Two sources of mesoscopic current in response to microwaves: photovoltaic current (solid), which is asymmetric in field (i.e., symmetric and antisymmetric parts are the same size, and each half of the total variance), and rectification current, which has a larger symmetric part (dotted) than antisymmetric part (dot dashed). Experimental data shows reasonable agreement with slope and saturation.

through the dot. When the applied gate voltage is small compared to the gate voltage correlation length in conductivity (~10 mV), this current can be approximated as

$$I_{\text{rect}} = \frac{\alpha \cos(\phi)}{2} (V_g^{ac})^2 \frac{dg}{dV_g}$$

Rectification does not require particularly high frequencies, and is the dominant source of dc current resulting from ac gate voltage at MHz frequencies. Examples of rectification are seen in the top panels of Fig. 17 and 18.

In contrast, beyond the adiabatic regime, when the ac frequency becomes comparable to various relaxation times in the problem, a photovoltaic mechanism leading to dc currents becomes dominant. Photovoltaic effects are characterized by a lack of ±B symmetry, examples of which are seen in Figs. 17 and 18.

There is some subtlety regarding using symmetry do disentangle rectification and photovoltaic effects: At intermediate microwave frequencies, conductance remains symmetric while the induced dc current becomes asymmetric. It higher frequencies, or larger amplitudes of microwave gate excitation, conductance becomes asymmetric as well, resulting in asymmetric rectification. In this regime separating photovoltaic and rectification effects cannot rely on magnetic field symmetry.